# Strong Fano effect in the magnetic circular dichroism of the Pt $N_{6,7}$ core absorption of ferromagnetic $CoPt_3$

T. Shishidou,* S. Imada, T. Muro, F. Oda, A. Kimura,† and S. Suga
*Department of Material Physics, Faculty of Engineering Science, Osaka University, 1-3 Machikaneyama, Toyonaka, Osaka 560, Japan*

T. Miyahara
*Photon Factory, National Laboratory for High-Energy Physics, Oho 1-1, Tsukuba-shi, Ibaragi 305, Japan*

T. Kanomata
*Department of Applied Physics, Faculty of Technology, Tohoku Gakuin University, Tagajo, Miyagi 985, Japan*

T. Kaneko
*Institute for Materials Research, Tohoku University, Katahira, Sendai 980, Japan*
(Received 10 September 1996)

We report the core photoabsorption (XAS) and magnetic circular dichroism (MCD) spectra in the Pt $N_{6,7}(4f \rightarrow 5d)$ region of the ferromagnetic $CoPt_3$. The measured XAS spectra have shown typical Fano line shapes, and the MCD spectrum has shown very unusual features that cannot be explained within the framework of the conventional selection rule for the dipole transition. It is revealed from a theoretical analysis that the strong Fano effect is essential to interpret these MCD features. We will discuss in detail the influence of the Fano effect on the Pt $N_{6,7}$ MCD line shape. [S0163-1829(97)03306-7]

## I. INTRODUCTION

The ordered alloys $MPt_3$ ($M$=V, Cr, Mn, Fe, Co) have a $Cu_3Au$-type crystal structure and have attracted much interest due to their wide variety of magnetic properties. In these intermetallic compounds, the Pt sites have induced magnetic moments due to the hybridization with the spin-polarized $3d$ states of transition metal sites. $VPt_3$ (Ref. 1) and $CrPt_3$ (Refs. 2 and 3) reveal ferrimagnetic ordering in the sense that the moment on the Pt sites is antiparallel to that on the $3d$ transition metal sites. $MnPt_3$ (Refs. 3 and 4) and $CoPt_3$ (Ref. 5) are ferromagnets, whereas $FePt_3$ (Ref. 6) shows antiferromagnetic ordering. The contribution of the orbital moment to the total moment on the Pt sites is expected to be important, because the Pt atom is so heavy (atomic number $Z$=78) that the spin-orbit coupling of the Pt $5d$ electrons is fairly large (coupling constant $\zeta_{5d} \simeq 0.5$ eV). It is interesting to investigate the variation of both $\langle L_z \rangle$ (the orbital angular momentum) and $\langle S_z \rangle$ (spin) on the Pt sites through the series of $MPt_3$ to reveal the origin of their rich variety of magnetic orderings. Maruyama *et al.*[7,8] have measured MCD spectra of $MPt_3$ ($M$=Cr, Mn, Co) and ferromagnetic $Fe_3Pt$ (Ref. 9) in the Pt $L_{2,3}$ edges ($2p \rightarrow 5d$ transition by hard x ray). Using the magneto-optical sum rules,[10,11] they have shown interesting variations of $\langle L_z \rangle$ and $\langle S_z \rangle$ on the Pt site. In $CrPt_3$, the $\langle L_z \rangle$ component dominates the magnetic moment on the Pt site, contrastingly, it disappears in $MnPt_3$. In the case of $CoPt_3$, the $\langle S_z \rangle$ contribution is predominant and the $\langle L_z \rangle$ is aligned parallel to the $\langle S_z \rangle$. Very recently, Iwashita *et al.*[12] have calculated the electronic band structures of $MPt_3$ by using the full-potential linear augmented plane wave (FLAPW) method with including the spin-orbit interaction as a perturbation. Their calculation reproduces the experimental trend of the $\langle L_z \rangle$ and $\langle S_z \rangle$ well. The orbital moment of Pt in $CoPt_3$ is, however, underestimated by a factor of about two.

In this paper, we report on the MCD spectrum of ferromagnetic $CoPt_3$ observed in the photon energy range of $\hbar\omega$ =50–80 eV. The observed MCD spectrum in the Pt $N_{6,7}(4f \rightarrow 5d)$ region has shown very unusual features. This MCD spectral shape deviates completely from the one expected by considering the conventional selection rule of the dipole transition. From a detailed theoretical analysis, it is found that the unusual line shape of the MCD is caused by a strong interference effect (Fano effect[13]) in the form of resonant photoemission.

In Sec. II, we describe the experimental results. In Sec. III, we present a theoretical framework and calculation done to explain the Pt $N_{6,7}$ MCD features of $CoPt_3$. Section IV is devoted to the concluding remarks.

## II. EXPERIMENTAL RESULTS

The polycrystalline sample of ferromagnetic $CoPt_3$ was prepared by the arc-melting technique from 99.9% pure Co and Pt in argon atmosphere. In order to develop the ordered arrangement of atoms, the cast was annealed for 5 weeks at 680 °C. An x-ray diffraction study showed the $Cu_3Au$-type ordered structure. The Curie temperature was 367 K and the total magnetic moment was measured to be $2.71\mu_B/CoPt_3$ at 4.2 K. From the result of neutron scattering,[5] it is known that the Pt site has an induced magnetic moment $M_{Pt}$ $=0.26\mu_B$/atom and the Co site has a moment $M_{Co}=1.64\mu_B$/atom at 77 K. It is believed that they are coupled ferromagnetically.

Core photoabsorption spectra (XAS) and MCD spectra in the range of $\hbar\omega$=50–80 eV were measured at the beamline BL28A (Ref. 14) of the Photon Factory in the National Laboratory for High Energy Physics (KEK). The circularly

 

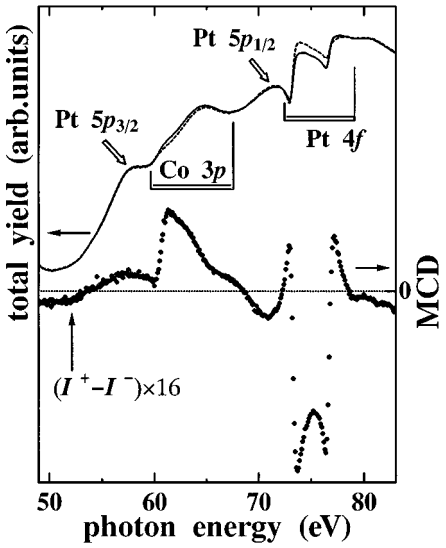


FIG. 1. Core absorption (XAS) and MCD spectra of $CoPt_3$ in the photon energy range $\hbar\omega$=50–80 eV. The solid and dashed curves show the XAS spectra, $I^+$ and $I^-$, measured by means of the total photoelectron yield method. The dots show the MCD spectrum, $I^+ - I^-$. The horizontal dotted line represents the MCD zero.

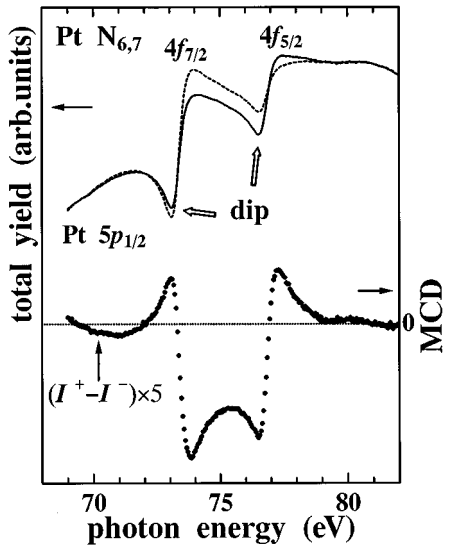


FIG. 2. Detailed XAS and MCD spectra taken in the Pt $4f \rightarrow 5d$ excitation region. The XAS shows asymmetric Fano line shape and the MCD spectrum reveals very unusual features. See text for details.

polarized light was supplied by a helical undulator. Almost completely polarized light was obtained at the peak of the first harmonic of the undulator radiation. The full bandwidth of the monochromatized incident photons was set to about 0.1 eV. A clean sample surface was obtained by in situ scraping with using a diamond file under ultrahigh vacuum condition ($\simeq 1\times 10^{-9}$ Torr). The sample was cooled down by liquid $N_2$. A magnetic field of about 1.1 T was applied to the sample by using an apparatus with two sets of permanent dipole magnets[15] made of Nd-Fe-B alloy. XAS spectra were measured by the total photoelectron yield (TPY) method by directly measuring the sample current while scanning the photon energy ($\hbar\omega$). It is widely known that the TPY spectrum well represents the photoabsorption in the core excitation region. MCD spectra were taken by reversing the direction of the magnetic field $\boldsymbol{H}$ applied to the sample at each $\hbar\omega$ while the helicity of the light was fixed. We define the MCD spectrum as $I^+ - I^-$, where $I^+$ and $I^-$ denote the absorption intensity with the photon spin (helicity) parallel and antiparallel to the direction of the applied magnetic field, respectively (note that our definition of MCD is opposite to the one in Ref. 16.)

The experimental results obtained in the photon energy range of $\hbar\omega$=50–80 eV are shown in Fig. 1. Here the solid and dashed curves represent the XAS spectra, $I^+$ and $I^-$, respectively, and the dots show the MCD spectrum. One recognizes rather broad peaks in the XAS, which originate from the core excitations of the Pt $5p_{3/2}$, Co $3p$, Pt $5p_{1/2}$, and Pt $4f$ states as indicated in the figure. Clear MCD signals are seen near each edge. The Pt $5p \rightarrow 5d$ XAS shows a large spin-orbit splitting ($\simeq$13 eV) with a *positive* and a *negative* MCD signals in the regions of the $5p_{3/2}$ and $5p_{1/2}$ components, respectively. Considering the selection rule for the $p \rightarrow d$ dipole transition, we confirm from these MCD signals that the magnetic moment on the Pt site ($\boldsymbol{M}_{\mathrm{Pt}}$) is aligned parallel to the applied magnetic field ($\boldsymbol{H}$), $\boldsymbol{M}_{\mathrm{Pt}} \| \boldsymbol{H}$. The magnetic moment on the Co site is confirmed to be parallel to $\boldsymbol{H}$, because $\boldsymbol{M}_{\mathrm{Co}}(1.64\mu_{\mathrm{B}}/\mathrm{atom})$ dominates the total magnetic moment of $CoPt_3$. Therefore, we can reach a conclusion that $\boldsymbol{M}_{\mathrm{Pt}} \| \boldsymbol{M}_{\mathrm{Co}}$, which is consistent with the neutron scattering result.[5]

Noticeable MCD signals are observed in the higher energy region where the Pt $4f \rightarrow 5d$ absorption ($4f$ XAS) arises. We have carried out a detailed measurement of the Pt $4f$ MCD in the narrow photon energy range of $\hbar\omega$=70–80 eV. The results are shown in Fig. 2. In the $I^+$ and $I^-$ XAS spectra, one can see broad peaks related to the $4f_{7/2}$ and $4f_{5/2}$ components at about 74 and 77.5 eV. In the prethreshold regions of both components, clear dips are observed. As a result, the XAS spectrum has a very asymmetric line shape. It is well known that such a characteristic line shape is caused by the Fano effect.[13,17] The MCD spectrum displayed in the lower panel of Fig. 2 also shows characteristic features. Considering the direction of the Pt moment ($\boldsymbol{M}_{\mathrm{Pt}} \| \boldsymbol{H}$) and the selection rule for the $f \rightarrow d$ dipole transition, one expects that the MCD signal should become negative in the $4f_{7/2}$ and positive in the $4f_{5/2}$ region. The observed MCD spectrum deviates considerably from such an expectation and shows very unusual features, namely, a *positive* and a *negative* MCD signals in the $4f_{7/2}$ region with increasing $\hbar\omega$, and a *negative* and a *positive* signals in the $4f_{5/2}$ region. As a whole, the MCD line shape is well represented by the letter ''W.'' It is known that the Fano effect gives rise to some characteristic features in MCD spectra. Muto *et al.*[18,19] have measured MCD spectra in the $M_{2,3}$ ($3p \rightarrow 3d$) edge of Ni metal and in the $N_{4,5}$ ($4d \rightarrow 4f$ ) edge of rare-earth metals. In such a shallow core excitation, the Fano effect is not negligible and they observed characteristic ''extended MCD'' features. The overall line shape of their MCD, however, is well understood within the framework of ordinary $p \rightarrow d$ (Ni) or $d \rightarrow f$ (rare-earth) dipole transition. In the case of the present Pt $4f$, the MCD line shape cannot even be qualitatively explained in the framework of the dipole selection

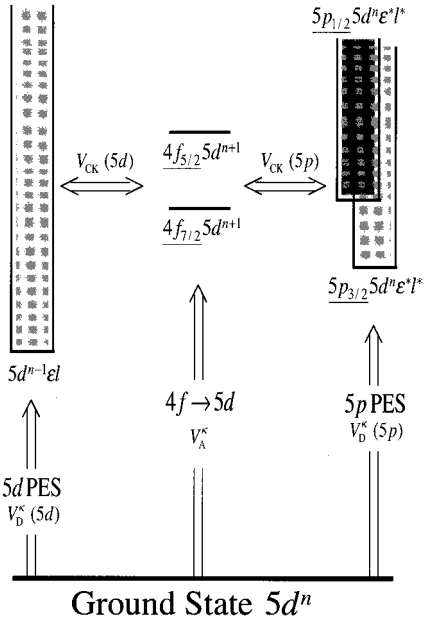


FIG. 3. A conceptual diagram representing the interactions in the Pt $4f$ XAS process. The vertical axis represents the total energy of the system. In addition to the $4f \rightarrow 5d$ dipole transition ($4f$ XAS), the $5d$ PES and $5p$ PES processes also occur. There is a configuration interaction between the discretelike excited states and continuum states via the CK transitions, which leads to the Fano-type interference effect.

rule. We suppose that an extremely strong Fano effect may be the origin of this unusual MCD. In the following section, we present basic concepts to treat this problem and perform a simplified theoretical calculation in order to discuss the influence of the Fano effect on the Pt $4f$ MCD spectrum.

### III. DISCUSSION

The basic concepts concerned about the Fano effect in the Pt $N_{6,7}$ region are schematically illustrated in Fig. 3. First we regard the electron configuration of the Pt in the ground state as $5d^n$. The Pt $4f$ XAS leads to the quasidiscrete excited states $4f^{13}5d^{n+1}$. On the other hand, the Pt $5d$ photoemission [$5d$ valence photoemission spectroscopy (PES)] process always occurs at any $\hbar\omega$, producing the $5d^{n-1}\epsilon l$ continuum states. Here, $\epsilon l$ denotes the photoelectron state with energy $\epsilon$ and the orbital angular momentum $l$ ($l=p$ or $f$). The Pt $5p$ core level lies in the energy region between the $4f$ core and the $5d$ valence states, so that the $5p$ PES process also takes place for a photon energy corresponding to the $4f$ XAS excitation, resulting in the $5p^5 5d^n \epsilon^* l^*$ continuum states ($l^*=s$ or $d$). The discretelike excited states ($4f^{13}5d^{n+1}$) are embedded in the various continua and will interact with them by Coster-Krönig transitions ($\underline{4f}5d5d$ and $\underline{4f}5p5d$ CK transitions). From these configuration interactions, the $4f$ XAS process ($4f \rightarrow 5d$), which is followed by the CK decay, will interfere with the direct PES processes and will lead to the asymmetric Fano line shape.

In order to clarify how the Fano effect works on the Pt $4f$ MCD spectrum of $CoPt_3$, we perform a simplified calculation in this section. The Fano effect is essentially an intra-atomic phenomenon, so that the information about the local electronic and magnetic states projected to one Pt site is needed. The Anderson impurity model is suitable for this purpose. We pick out one Pt atom which will be photoexcited and regard this atom as an impurity that has an *atomic* $5d$ orbital. The electronic states constructed by other Co and Pt atoms are considered to be Bloch states which would be well described by the band structure calculation. We regard these Bloch states as ''electron reservoir orbitals'' (hereafter denoted by $v$). We assume a hybridization between the impurity $5d$ orbital and $v$. Due to this hybridization, the impurity Pt would have a magnetic moment, reflecting the spin-polarized DOS of the reservoir state. The ground state of the system $|g\rangle$ is assumed to be symbolically expressed as

$$|g\rangle = c_1|5d^{10}\rangle + c_2|5d^9 v\rangle. \tag{1}$$

Here, $|5d^{10}\rangle$ denotes the state where the impurity Pt has the $5d^{10}$ configuration and the reservoir states below the Fermi energy are occupied, and $|5d^9 v\rangle$ is the state which can be created from $|5d^{10}\rangle$ by transferring one of the $5d$ electrons into the empty reservoir state above the Fermi energy. Other configurations ($5d^8 v^2$, etc.) and the bandwidth of the unoccupied reservoir states are tentatively neglected. The point group symmetry around the Pt atom is assumed as $O_h$ for simplicity although it is actually $D_{4h}$ in $CoPt_3$. The Hamiltonian of the system is expressed as

$$H = \sum_{\mu} \epsilon_d n_{d_\mu} + \frac{1}{2} U_{dd} \sum_{\mu \neq \mu'} n_{d_\mu} n_{d_{\mu'}} + H_d(\zeta_d) + H_f(\zeta_f) + \sum_{\sigma} \sum_{i} V_{\Upsilon_i}(\sigma) \sum_{\gamma_i} (a^+_{d_{\gamma_i \sigma}} a_{v_{\gamma_i \sigma}} + \text{H.c.}). \tag{2}$$

In Eq. (2), the origin of energy is taken at the reservoir level (Fermi energy). The first term represents the one-body energy of the $5d$ states. Here, $\mu$ denotes the combined index specifying the $5d$ magnetic quantum number and spin state. The second term represents the $5d$-$5d$ repulsive Coulomb interaction. The third and fourth terms represent the spin-orbit interaction of the $5d$ (with a coupling constant $\zeta_d$) and $4f$ core states ($\zeta_f$), respectively. We use the Hartree Fock values $\zeta_d = 0.52$ eV and $\zeta_f = 1.00$ eV. The last term expresses the hybridization between the impurity $5d$ and reservoir states. The index $\sigma$ denotes the spin state and the index $\gamma_i$ runs over the basis of the $\Upsilon_i$ ($t_{2g}$ or $e_g$) irreducible representation of the $O_h$ group. The empirical relation $V_{e_g} = -2V_{t_{2g}}$ is assumed. The spin-dependent hybridization strength is considered to be related to the reservoir DOS by the relation of $V^2(\sigma) \propto \text{DOS}(\sigma)$.[20] According to the LAPW band structure calculation of $CoPt_3$,[21] the total DOS at the Fermi energy (constructed mainly by the Co $3d$ and Pt $5d$ states) shows the ratio of DOS(down)/DOS(up)$\simeq$0.45 (the majority spin is the down spin in our definition), and we assume $V(\text{down}) = 0.7 \times V(\text{up})$. Let us define the average energy difference between the two configurations as $\Delta = E(5d^{10}) - E(5d^9 v)$. It may be clear that $\Delta$ is positive because the Pt $5d$ electron number is close to 9 according to the band structure calculation. The free parameters in Eq. (2) are only $\Delta$ and $V_{e_g}(\uparrow)$. We choose the parameters so as to obtain the total magnetic moment $\langle M_z \rangle = -(2\langle S_z \rangle + \langle L_z \rangle) = 0.26\mu_B$, that is the Pt moment observed by neutron

TABLE I. The ground-state properties calculated with varying the parameter $\Delta \equiv E(5d^{10}) - E(5d^9 v)$. We chose $V_{e_g}(\uparrow)$ so as to obtain $\langle M_z \rangle = 0.26 \mu_B$.

| $\Delta$ (eV) | 1.0 | 1.5 | 2.0 | 2.5 | 3.0 |
|---|---|---|---|---|---|
| $V_{e_g}(\uparrow)$(eV) | 1.60 | 1.95 | 2.25 | 2.55 | 2.80 |
| $n_{5d}$ | 9.40 | 9.39 | 9.38 | 9.37 | 9.36 |
| $\langle L_z \rangle / \langle S_z \rangle$ | 0.705 | 0.605 | 0.543 | 0.492 | 0.459 |

scattering.[5] From this restriction the number of the free parameters is reduced to only one, so that we treat $\Delta$ as the free parameter. In Table I, we show the calculated ground-state properties with varying $\Delta$. For larger $\Delta$, both $n_{5d}$ (the $5d$ electron number, $\langle g | \Sigma_\mu n_{d_\mu} | g \rangle$) and $\langle L_z \rangle / \langle S_z \rangle$ become smaller.

We briefly explain the photoexcitation processes. Discretelike $\underline{4f}/5d^{10}\underline{v}$ states will be excited by the $4f \rightarrow 5d$ dipole transition from the ground state given by Eq. (1). We call these states the *intermediate* states because they will soon decay into various *final* states by the Coster-Krönig transitions as shown in Fig. 3. Eigenvalues and eigenfunctions of the intermediate states are denoted as $E_m$ and $|m\rangle$, respectively. The final states can be reached not only via the intermediate states but also directly from the ground state by the $5d$ PES and $5p$ PES processes. Their eigenvalues and eigen functions are denoted as $E_{f\epsilon}$ and $|f\epsilon\rangle$. We ignore the interaction between the photoelectron and the rest of the system, so that $|f\epsilon\rangle$ can be expressed as a direct product $|f\epsilon\rangle = |f\rangle |e\rangle$ with $E_{f\epsilon} = E_f + \epsilon$; here $|\epsilon\rangle$ denotes the photoelectron state and $|f\rangle$ is the eigenstate of the rest of the system (symbolically, $|f\rangle = c_1' |5d^9\rangle + c_2' |5d^8 v\rangle + c_3' |\underline{5p} 5d^{10}\rangle + c_4' |\underline{5p} 5d^9 v\rangle$).

We calculate the Pt $N_{6,7}$ XAS spectrum using the $T$ matrix which is generally applied in the calculation of excitation spectra with interference effect.[22] Our $T$ matrix is defined as

$$T(\omega) = V + V \frac{1}{z - H - H_{\rm pe} - V} V. \tag{3}$$

Here, $z = \omega + E_g + i\tau$ $(\tau \rightarrow +0)$, $\omega$ is the incident photon energy, $E_g$ is the energy of the ground state $|g\rangle$, $H$ is given by Eq. (2), and $H_{\rm pe}$ is the Hamiltonian of a photoelectron $(H_{\rm pe} |\epsilon\rangle = \epsilon |\epsilon\rangle)$. Based on the concepts illustrated in Fig. 3, the perturbation $V$ is given by

$$V = V_A^\kappa + V_D^\kappa + V_{\rm CK} + {\rm H.c.} \tag{4}$$

The superscript $\kappa$ denotes the photon helicity $(\kappa = \pm 1)$. The operator $V_A^\kappa$ is to represent the $4f \rightarrow 5d$ dipole transition ($4f$ XAS) which is expressed by the dipole matrix element $\langle 4f | r | 5d \rangle$. The operator $V_D^\kappa$ represents the direct photoemission processes. $V_D^\kappa$ consists of two parts, $V_D^\kappa = V_D^\kappa(5d) + V_D^\kappa(5p)$, where the two operators are described with the use of the matrix element $\langle 5d | r | \epsilon l \rangle$ and $\langle 5p | r | \epsilon^* l^* \rangle$, respectively. The operator $V_{\rm CK}$ likewise represents the Coster-Krönig (CK) transitions, $V_{\rm CK} = V_{\rm CK}(5d) + V_{\rm CK}(5p)$, where $V_{\rm CK}(5d)$ and $V_{\rm CK}(5p)$ describe the $\underline{4f} 5d \underline{5d}$ and $\underline{4f} 5p \underline{5d}$ CK decays expressed with the use of the radial integrals $R^k(5d, 5d; 4f, \epsilon l)$ and $R^k(5p, 5d; 4f, \epsilon^* l^*)$, respectively. We calculate the $T$ matrix by taking into account the perturbation up to the lowest order of $V_A^\kappa$ and $V_D^\kappa$, and to infinite orders of $V_{\rm CK}$. Although the operators $V_{\rm CK}$ and $V_D^\kappa$ are actually depending on the photoelectron kinetic energy $\epsilon$, we disregard their $\epsilon$ dependences for simplicity. After some algebra,[22] the $T$ matrix is expressed as

$$T(\omega) = (V_A^{\kappa +} - i\pi V_D^{\kappa +} V_{\rm CK}) \frac{1}{z - H_m + i\Gamma} (V_A^\kappa - i\pi V_{\rm CK}^+ V_D^\kappa) - i\pi V_D^{\kappa +} V_D^\kappa. \tag{5}$$

Here, $H_m$ is the Hamiltonian of the intermediate state $(H_m |m\rangle = E_m |m\rangle)$, and $\Gamma = \pi V_{\rm CK}^+ V_{\rm CK}$. The absorption spectrum $I^\kappa(\omega)$ is given by the optical theorem as

$$I^\kappa(\omega) = -\frac{1}{\pi} {\rm Im} \langle g | T(\omega) | g \rangle. \tag{6}$$

We should first evaluate various matrix elements listed in Table II. The radial part of the one-electron wave function $\psi_{nlm\sigma}(r, \theta, \phi) = [P_{nl}(r)/r] Y_{lm}(\theta, \phi) \chi(\sigma)$ is evaluated from the nonrelativistic atomic Hartree Fock approximation.[23] The radial wave function of the continuum state is obtained from the following differential equation[24] in the units of Rydberg and Bohr radius:

$$\left[ -\frac{d^2}{dr^2} + \frac{l(l+1)}{r^2} + V^{\epsilon l}(r) \right] P_{\epsilon l}(r) = \epsilon P_{\epsilon l}(r). \tag{7}$$

The normalization condition is

$$P_{\epsilon l}(r) \xrightarrow{r \rightarrow \infty} \pi^{-1/2} \epsilon^{-1/4} \otimes \sin[\epsilon^{1/2} r - l\pi/2 - \epsilon^{-1/2} \ln(2\epsilon^{1/2} r) + \delta_l],$$

where $\delta_l$ is a phase shift. The potential $V^{\epsilon l}$ may be expressed as[24]

$$V^{\epsilon l}(r) = -2Z/r + V_H(r) - [24\rho(r)/\pi]^{1/3}. \tag{8}$$

Here the second term is the Hartree potential energy in the field of the $N-1$ bound electrons. The third term represents the exchange energy with the bound electrons of the electron-density $\rho(r)$. $V^{\epsilon l}(r)$ was evaluated with using the nonrelativistic HF radial wave functions of the bound electrons, and Eq. (7) was solved. The absolute values of the evaluated $\langle 5d | r | \epsilon l \rangle$ and $\langle 5p | r | \epsilon^* l^* \rangle$ were, however, too small to explain the interference effect. We suppose that this failure comes from the nonrelativistic treatment of the bound electrons. The Pt atom is rather heavy $(Z = 78)$, so that the core $s$ and $p$ electrons would be relativistically contracted toward the nucleus and the nuclear attractive potential $-2Z/r$ would be strongly shielded.[25] So, relativistic effects should be taken into account. Being based on the local density approximation (LDA), the scalar-relativistic LAPW potential $V_{\rm APW}(r)$ of $CoPt_3$,[26] was employed as the potential $V^{\epsilon l}(r)$. It is known that a bold approximation of LDA in the treatment of the exchange-correlation term induces a wrong behavior of $V_{\rm APW}(r)$ for large $r$. Namely $V_{\rm APW}$ descreases very fast (exponentially) whereas it should behave as $-2/r$ for large $r$ in the units of Rydberg and Bohr radius. In order to eliminate such a shortcoming, $V_{\rm APW}$ is modified as

TABLE II. Values of the matrix elements evaluated by using the HF radial wave functions for the bound states and the modified LAPW potential for continuum (See text for details). The employed units are $a_0$ (Bohr radius) for $\langle 4f|r|5d\rangle$, $a_0/\sqrt{\text{eV}}$ for other dipole matrix elements and $\sqrt{\text{eV}}$ for $R^k$'s. We chose the kinetic energy of the continuum electron as $\epsilon$=70 eV and $\epsilon^*$=10 eV.

$\langle 4f|r|5d\rangle = 0.2235$
$\langle 5d|r|\epsilon p\rangle = 0.02907$ $\quad$ $\langle 5p|r|\epsilon^* s\rangle = 0.07415$
$\langle 5d|r|\epsilon f\rangle = 0.07636$ $\quad$ $\langle 5p|r|\epsilon^* d\rangle = -0.1176$

| | direct | | | exchange | | |
|---|---|---|---|---|---|---|
| $R^k(5d,5d;4f,\epsilon l)$ | | | | | | |
| | $k=1$ | $k=3$ | $k=5$ | | | |
| $l=p$ | 0.02960 | −0.001095 | | | | |
| $l=f$ | −0.2195 | −0.1568 | −0.1091 | | | |
| $l=h$ | | 0.03723 | 0.02034 | | | |
| $R^k(5p,5d;4f,\epsilon^* l^*)$ | | | | | | |
| | $k=2$ | $k=4$ | | $k=1$ | $k=3$ | $k=5$ |
| $l^*=s$ | 0.005459 | | | −0.01083 | | |
| $l^*=d$ | −0.3443 | −0.2369 | | −0.3161 | −0.2466 | |
| $l^*=g$ | −0.01590 | −0.005665 | | | −0.005082 | −0.003086 |

$$rV^{\epsilon l}_{\text{APW}}(r) = \begin{cases} rV_{\text{APW}}(r) & (\text{if } rV_{\text{APW}} \leqq -2) \\ -2 & (\text{otherwise}). \end{cases} \tag{9}$$

As for the bound states' radial wave functions $P_{5d}$, $P_{5p}$, and $P_{4f}$ which appear in the required matrix elements, we tentatively used the nonrelativistic atomic HF radial wave functions (for $P_{5d}$, the HF result is almost the same as the LAPW radial wave function except for the behavior near the muffin-tin radius where the contribution of the neighboring muffin-tin sphere takes place). The matrix elements obtained by this way are listed in Table II. In the calculation of the spectra, the values of $R^k$ are reduced to 80% of the values in Table II in order to match the experimental spectral broadening.

Maruyama *et al.* have so far estimated the ratio $\langle L_z\rangle/\langle S_z\rangle$ of the Pt site of $CoPt_3$ as being about 0.6.[8] In our theoretical framework, the same value of $\langle L_z\rangle/\langle S_z\rangle$ is obtained by choosing the parameter $\Delta$=1.5 eV (See Table I). Starting from this ground state, let us examine how the Fano effect works on the MCD spectrum. For this purpose, we introduce a coefficient $Q_D$ which scales the dipole matrix elements of the direct photoemission processes as $Q_D\langle 5d|r|\epsilon l\rangle$ and $Q_D\langle 5p|r|\epsilon^* l^*\rangle$. When $Q_D$ equals zero, there is no direct photoemission process so that the interference effect does not occur. As we increase $Q_D$ from zero, the Fano effect would become gradually stronger. The results calculated with varying $Q_D$ are shown in Fig. 4. The polarization-averaged XAS spectra, $(I^+ + I^-)/2$, are presented in the upper panel of the figure, and the MCD spectra, $I^+ - I^-$, are shown in the lower panel. In the case of $Q_D$=0, the XAS shows a simple two peak structure. Both $4f_{7/2}$ and $4f_{5/2}$ components show symmetric Lorentzian line shapes. For a finite $Q_D$, the XAS has an asymmetric line shape with a dip and a noticeable tail. For larger $Q_D$, these features are enhanced and the absorption peak moves to higher photon energies. The MCD spectrum also shows an interesting variation. For $Q_D$=0, the MCD spectrum shows a negative (denoted as ''$A$'' in the figure) and a positive (''$B$'') peak in the $4f_{7/2}$ and $4f_{5/2}$ region, respectively, as expected from the dipole selection rule. For larger $Q_D$, peak $A$ becomes stronger and peak $B$ becomes weaker. Both peaks shift to higher energies and additional structures $A'$ and $B'$ appear in the lower energy region of peaks $A$ and $B$, respectively. A reasonable agreement with the experimental result is obtained by choosing the value of $Q_D$=0.4 as shown in Fig. 5. Here the dotted curves represent the experimental results and the solid curves represent the calculated results. A monotonously increasing background is subtracted from the experimental absorption spectrum. Although the calculated absorption spectrum reproduces the asymmetric Fano line shape well, a discrepancy can be seen in the region of absorption peaks. Namely the calculated spectrum is rather sharp compared to the experimental spectrum. As for the MCD spectrum, the calculation reproduces

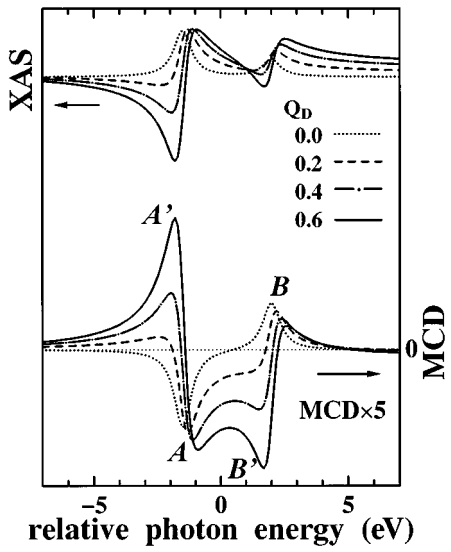


FIG. 4. The calculated results obtained with fixing $\Delta$=1.5 eV ($\langle L_z\rangle/\langle S_z\rangle$=0.6) and varying $Q_D$. In the upper panel the polarization-averaged XAS spectra $(I^+ + I^-)/2$ are shown. The lower panel shows the MCD spectra $I^+ - I^-$. The results for $Q_D$=0, 0.2, 0.4, and 0.6 are represented by the dotted (···), dashed (---), dot-dashed (-·-), and the solid (—) curves.

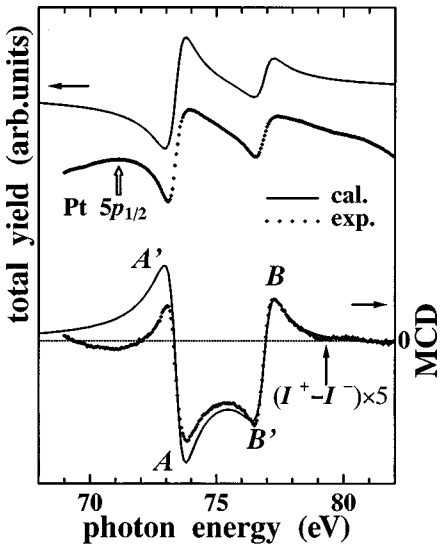


FIG. 5. A comparison between the experimental (dots) and the best fit calculated (solid curves) results ($Q_D=0.4$ with the ground state $\Delta=1.5$ eV).

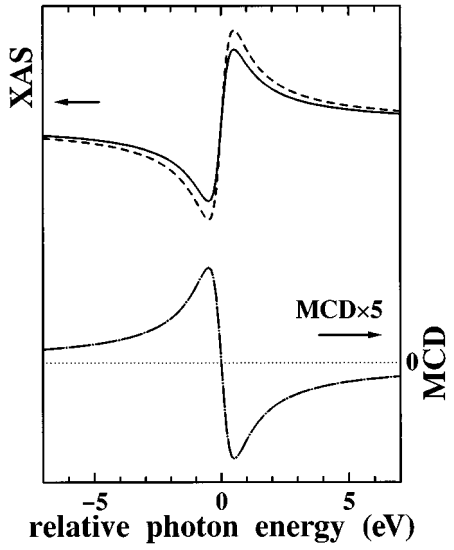


FIG. 6. An example of the spectrum of the interference term $D(\omega)F_3(\kappa)$. Considering the $4f_{7/2}$ edge, we set $F_3(+1)=0.8$, $F_3(-1)=1.0$, and $\Gamma=0.5$ eV. See text for details.

peaks $B$ and $B'$ fairly well, whereas a deviation is seen around peaks $A$ and $A'$ in the sense that the amplitude of the calculated spectrum is too large. The negative MCD signal of the Pt $5p_{1/2}$ component, not taken into account in the present calculation, may partly cancel the positive MCD of the $A'$ peak. The possibility of another major reason for this discrepancy will be discussed later.

Thus the unusual MCD line shape of the Pt $4f$ XAS in $CoPt_3$ can be qualitatively understood from the spectral function of Eqs. (6) and (5). We will further inspect the details with taking the $4f_{7/2}$ region as an example. With the use of the intermediate state eigen functions $|m\rangle$ belonging to the $\underline{4f_{7/2}}5d^{10}\underline{v}$ configuration, and with the assumption of a constant $\Gamma$, Eq. (6) can be resolved into the following four terms:

$$I^{\kappa}(\omega)=\frac{1}{\pi}L(\omega)\sum_m |\langle m|V_A^{\kappa}|g\rangle|^2 - \pi L(\omega)\sum_m |\langle m|V_{\mathrm{CK}}^{+}V_D^{\kappa}|g\rangle|^2 + D(\omega)\sum_m \langle g|V_A^{k+}|m\rangle\langle m|V_{\mathrm{CK}}^{+}V_D^{\kappa}|g\rangle + \langle g|V_D^{\kappa+}V_D^{\kappa}|g\rangle. \quad (10)$$

Here, $L(\omega)$ is the Lorentzian function, $L(\omega)=\Gamma/(\omega^2+\Gamma^2)$. The function $D(\omega)=2\omega/(\omega^2+\Gamma^2)$ becomes zero at $\omega=0$ and has extremum values $\pm 1/\Gamma$ at $\omega=\pm\Gamma$. Note that the origin of $\omega$ is taken at $E_m-E_g$. The functions $L(\omega)$ and $D(\omega)$ determine the $\omega$ (photon energy) dependence of each term in Eq. (10). The fourth term represents the direct photoemission processes which just produce a background for both XAS and MCD in the present framework. The first term represents the *normal* photoabsorption process $4f\rightarrow 5d$, in which $F_1(\kappa)\equiv\Sigma_m|\langle m|V_A^{\kappa}|g\rangle|^2$ gives a negative MCD signal in the $4f_{7/2}$ region according to the dipole selection rule, leading to $F_1(+1)<F_1(-1)$. The second term represents a ''virtual'' process, in which the system is first excited from the ground state into the continuum states (where either $5p$ or $5d$ electron is excited) and then goes to the intermediate states by the reverse process of the CK decay (where the excited electron decays nonradiatively and the $4f$ electron is excited to the $5d$ state). Let us call this the *second order* process in the sense that the system follows the two sequential paths to reach the state $|m\rangle$. This second term contains the operator $V_D^{\kappa}$ and thus is proportional to $Q_D^2$. It has the same $\omega$ dependence as the first term [due to the Lorentzian $L(\omega)$]. In this term $F_2(\kappa)\equiv\Sigma_m|\langle m|V_{\mathrm{CK}}^{+}V_D^{\kappa}|g\rangle|^2$ which determines the $\kappa$ (helicity) dependence of the second term, has the same dependence as the first term, namely, $F_2(+1)<F_2(-1)$. The first and the second terms have signs opposite to each other and the sum of the two terms is almost canceled out at any $\omega$ for $Q_D=0.4$ (the best fit value). As the result, the third term almost determines the spectral shape of both the XAS and MCD. This term contains both the *normal* absorption process and the *second order* process and is called an *interference* term. This has a unique $\omega$ dependence, represented by $D(\omega)$, whereas the $\kappa$ dependence represented by $F_3(\kappa)\equiv\Sigma_m\langle g|V_A^{\kappa+}|m\rangle\langle m|V_{\mathrm{CK}}^{+}V_D^{\kappa}|g\rangle$ is the same as the preceding two terms. Namely, $F_3(+1)<F_3(-1)$ is realized. In Fig. 6 we show the behavior of the function $D(\omega)F_3(\kappa)$ on the supposition of $F_3(+1)=0.8$, $F_3(-1)=1.0$, and $\Gamma=0.5$ eV. In the upper panel of the figure, the solid (dashed) curve represents the spectrum for $\kappa=+1(-1)$. The dotted chain curve in the lower panel represents the MCD spectrum $D(\omega)[F_3(+1)-F_3(-1)]$. We recognize that a positive and a negative MCD signals reproduce the experimental result in the $4f_{7/2}$ region well. The MCD in the $4f_{5/2}$ region is likewise reproduced by this treatment. From this inspection it becomes clear that the observed unusual MCD features in the Pt $N_{6,7}$ region are just reflecting the $\omega$ and $\kappa$ dependence of the *interference* term.

The present theoretical approach has, however, two shortcomings. First of all, we obtained the best fit result by setting $Q_D=0.4$ (See Figs. 4 and 5), starting from the reasonable

ground state. The spectrum with $Q_D=1.0$ (not shown) cannot explain the experimental result because the peaks $A'$ and $B'$ become extremely enhanced. This suggests that our estimation of the dipole matrix elements $\langle 5d|r|\epsilon l\rangle$ and $\langle 5p|r|\epsilon^* l^*\rangle$ is not satisfactory. A full relativistic HF treatment may reduce this disagreement. Secondly, the best fit result with $Q_D=0.4$ still has some discrepancies around the peak $A$ and $A'$. These discrepancies may be coming from the too simplified treatment of the continuum excitation processes. As shown in Fig. 3, three types of the continuum states, $5d^{n-1}\epsilon l$, $\underline{5p_{3/2}}5d^n\epsilon^* l^*$, and $\underline{5p_{1/2}}5d^n\epsilon^* l^*$, are considered. The intermediate states $\underline{4f}5d^{n+1}$ are assumed to interact with all kinds of continua. The $\underline{4f_{7/2}}5d^{n+1}$ intermediate states, however, may not be able to interact strongly with the continuum $\underline{5p_{1/2}}5d^n\epsilon^* l^*$ states. As shown in Fig. 1, the Pt $5p_{1/2}\rightarrow 5d$ absorption occurs around $\hbar\omega=72$ eV, and the largest part of the $5p_{1/2}\rightarrow\epsilon^* l^*$ continuum excitation absorption may be located at slightly higher energies than the Pt $4f_{7/2}\rightarrow 5d$ absorption onset. As a result, the $\underline{4f_{7/2}}5d^{n+1}$ states may not be heavily embedded in the $\underline{5p_{1/2}}5d^n\epsilon^* l^*$ continuum states. So the Fano effect around the photon energy of the $4f_{7/2}$ excitation threshold region would become much weaker compared to the present theoretical framework. Then the amplitude of the MCD around the $4f_{7/2}$ edge may be substantially reduced. These discrepancies should be removed in future.

Then we comment on magnetic sum rules.[10,11] We cannot simply apply the sum rules to the Pt $N_{6,7}$ MCD of $CoPt_3$, because the coexistence of the direct photoemission process and the interference effect are not considered in deriving the sum rules. So we should rely on the line shape fitting analysis to determine the ratio $\langle L_z\rangle/\langle S_z\rangle$. Figure 7 shows the calculated MCD spectra for a fixed $Q_D=0.4$ with varying the value of $\langle L_z\rangle/\langle S_z\rangle$ as 0.71 ($\Delta=1.0$ eV, solid curve), 0.49 (2.5 eV, dashed), and 0.29 (7.0 eV, dotted). The spectrum actually shows variation reflecting the change of the ground state. The MCD amplitude in the $4f_{5/2}$ region around the peak $B$ and $B'$ becomes larger when we reduce the value of $\langle L_z\rangle/\langle S_z\rangle$. This fact suggests that it may be possible to determine the ratio of $\langle L_z\rangle/\langle S_z\rangle$ from the line shape analysis. As we have seen in Fig. 4, however, the MCD is more sensitive to the change of $Q_D$ (the dipole matrix elements of the photoemission processes), so that the determination of $\langle L_z\rangle/\langle S_z\rangle$ from the line shape analysis is very difficult unless we accurately know the dipole matrix elements.

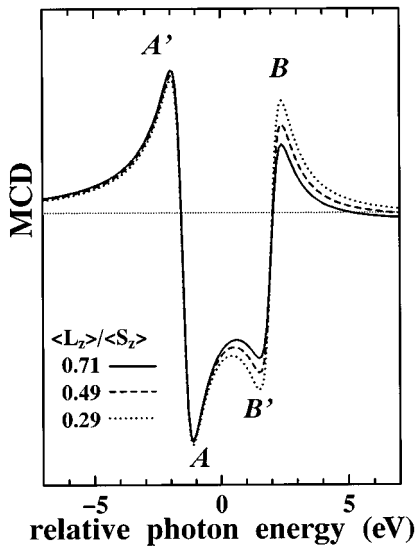


FIG. 7. Calculated MCD spectra for various ground states: $\langle L_z\rangle/\langle S_z\rangle=0.71$ ($\Delta=1.0$ eV, solid curve), 0.49 (2.5 eV, dashed), and 0.29 (7.0 eV, dotted). We fixed $Q_D=0.4$.

## IV. CONCLUSIONS

We have measured the XAS and MCD spectra in the Pt $N_{6,7}$ region of ferromagnetic $CoPt_3$. The measured XAS spectra show typical Fano line shapes with a clear dip, and the MCD spectrum reveals very unusual features unexpected from the dipole selection rule. From a theoretical analysis it becomes clear that the Fano effect is essential in both the XAS and MCD. A detailed inspection shows that the observed unusual MCD features are dominated by the photon energy and the polarization dependence of the interference term in the spectral function. A further elaborate theoretical approach is necessary in determining $\langle L_z\rangle/\langle S_z\rangle$ of the Pt moment. We should evaluate the accurate dipole matrix elements of the direct photoemission processes and treat the $\underline{5p}5d^n\epsilon^* l^*$ continuum excitation more precisely and take account of the real point group symmetry around the Pt site ($D_{4h}$) in the future.

## ACKNOWLEDGMENTS

The authors greatly appreciate Dr. A. Tanaka and Professor T. Jo of Hiroshima University for useful discussions and for giving information about computational techniques. The authors also thank Professor M. Shirai of Osaka University for providing the LAPW potential of $CoPt_3$ and Professor J. Ghijsen for revising the manuscript. The present work was partly supported by a Grant-in-Aid for Scientific Research from the Ministry of Education, Science and Culture.

*Present address: Department of Materials Science, Faculty of Science, Hiroshima University, Higashi-Hiroshima 739, Japan.

†Present address: Tsukuba Branch of Synchrotron Radiation Laboratory, Institute for Solid State Physics, University of Tokyo, Tsukuba-shi, Ibaragi 305, Japan.

[1] M. Kawakami and T. Goto, J. Phys. Soc. Jpn. **46**, 1492 (1979).

[2] S. K. Burke, B. D. Rainford, D. E. G. Williams, P. J. Brown, and D. A. Hukin, J. Magn. Magn. Mater. **15–18**, 505 (1980).

[3] S. J. Pickart and R. Nathans, J. Appl. Phys. **33**, 1336 (1962); *ibid.* **34**, 1203 (1963).

[4] B. Antonini, F. Lucari, F. Menzinger, and A. Paoletti, Phys. Rev. **187**, 611 (1969).

[5] F. Menzinger and A. Paoletti, Phys. Rev. **143**, 365 (1966).

[6] G. E. Bacon and J. Crangle, Proc. R. Soc. A **272**, 387 (1963).

[7] H. Maruyama, F. Matsuoka, K. Kobayashi, and H. Yamazaki, Physica B **208&209**, 787 (1995).

[8] H. Maruyama, F. Matsuoka, K. Kobayashi, and H. Yamazaki, J. Magn. Magn. Mater. **140–144**, 43 (1995).

[9] A. Z. Men'shikov, Yu. A. Dorofeev, V. A. Kazantsev, and S. K. Sidorov, Fiz. Met. Metall. **38**, 505 (1974).

[10] B. T. Thole, Paolo Carra, F. Sette, and G. van der Laan, Phys. Rev. Lett. **68**, 1943 (1992).
[11] Paolo Carra, B. T. Thole, Massimo Altarelli, and Xindong Wang, Phys. Rev. Lett. **70**, 694 (1993).
[12] K. Iwashita, T. Oguchi, and T. Jo, Phys. Rev. B **54**, 1159 (1996).
[13] U. Fano, Phys. Rev. **124**, 1866 (1961).
[14] Y. Kagoshima, S. Muto, T. Miyahara, T. Koide, S. Yamamoto, and H. Kitamura, Rev. Sci. Instrum. **63**, 1289 (1992).
[15] S. Muto, Y. Kagoshima, and T. Miyahara, Rev. Sci. Instrum. **63**, 1470 (1992).
[16] See, for example, C. T. Chen, F. Sette, Y. Ma, and S. Modesti, Phys. Rev. B **42**, 7262 (1990); C. T. Chen, Y. U. Idzerda, H.-J. Lin, N. V. Smith, G. Meigs, E. Chaban, G. H. Ho, E. Pellegrin, and F. Sette, Phys. Rev. Lett. **75**, 152 (1995).
[17] R. E. Dietz, E. G. McRae, and J. H. Weaver, Phys. Rev. B **21**, 2229 (1980).
[18] S. Muto, Y. Kagoshima, T. Miyahara, S. Yamamoto, and H. Kitamura, Solid State Commun. **83**, 41 (1992).
[19] S. Muto, S. Y. Park, S. Imada, K. Yamaguchi, Y. Kagoshima, and T. Miyahara, J. Phys. Soc. Jpn. **63**, 1179 (1994).
[20] J. W. Allen, S. J. Oh, O. Gunnarsson, K. Schönhammer, M. B. Maple, M. S. Torikachvili, and I. Lindau, Adv. Phys. **35**, 275 (1986).
[21] M. Shirai, H. Maeshima, and N. Suzuki, J. Magn. Magn. Mater. **140–144**, 105 (1995).
[22] A. Tanaka and T. Jo, J. Phys. Soc. Jpn. **63**, 2788 (1994).
[23] C. F. Fischer, Comput. Phys. Commun. **43**, 355 (1987).
[24] R. D. Cowan, *The Theory of Atomic Structure and Spectra* (University of California Press, Berkeley, 1981).
[25] R. D. Cowan and D. C. Griffin, J. Opt. Soc. Am. **66**, 1010 (1976).
[26] M. Shirai (private communication).